mater.scichina.com link.springer.com

Published online 30 June 2023 | https://doi.org/10.1007/s40843-023-2456-6
Sci China Mater 2023, 66(8): 3146–3154

Construction of $ZnIn_2S_4$/Sv-MoS_2 photocatalysts with subtle atomic-level intimate contacts: Enhancing interfacial interactions to improve photocatalytic H_2 evolution in visible light

Shihua Ye[1,2,3], Jingjun Li[1,2,3], Yanan Feng[1], Shuiying Gao[1,2,3*] and Rong Cao[1,2,3*]

ABSTRACT **The low charge separation efficiency between catalyst and cocatalyst severely limits the performance of photocatalysts. The strong interfacial interactions between catalyst and cocatalyst can improve the charge separation efficiency. Introducing interfacial chemical bonds to enhance the interfacial interaction between components is an effective way to improve photocatalytic performance. Herein, $ZnIn_2S_4$ (ZIS)/Sv-MoS_2 photocatalyst was synthesized. The binding effect between S atoms in ZIS and the uncoordinated Mo atoms in Sv-MoS_2 forms the interfacial Mo–S bond which greatly improves the photocatalytic activity of ZIS. The MoS_2-*x*h was prepared by $NaBH_4$ etching for different times. This extraordinary photocatalytic activity is mainly due to the easy transfer of photogenerated electrons from ZIS to MoS_2 *via* the heterojunction interface tightly connected under the action of Mo–S bonds. Photoelectric measurements show that ZIS/MoS_2-4h possesses effective charge transfer. This work reveals the effect of the introduction of interfacial chemical bonds on the photocatalytic activity of ZIS/MoS_2, and provides a simple and effective method for designing excellent cocatalysts through interface engineering.**

Keywords: Sv-MoS_2, $ZnIn_2S_4$, $NaBH_4$ etching, interfacial chemical bond, photocatalytic hydrogen evolution

INTRODUCTION

With the industrialization and fast development of economy, the energy shortages and atmospheric pollution become serious issues needed to be addressed [1–3]. Photocatalytic hydrogen production is an effective way to convert solar energy into clean energy [4–9]. Sulfides are excellent candidates for photocatalytic hydrogen production because they have suitable band gaps and conduction band [10–14]. However, the photocatalytic activity of sulfides is usually limited by the rapid recombination of photogenerated carriers and the lack of corresponding active sites. To address these issues, considerable efforts have been implemented to boost the photocatalytic activity of photocatalyst, such as element doping, heterostructure construction and cocatalyst loading. Many studies show that metal and nonmetal element doping significantly affect the photocatalytic activity of materials [15,16]. Recently, Ding's group [17] proposed that different doping depths of elements have great influence on charge transfer. It is difficult for a single-component photocatalyst to have a wide light absorption range, rapid charge separation and strong redox ability at the same time. By reasonably constructing heterojunction, the advantages of multiple components can be integrated [18–22]. Mao's group [23] designed a new photocatalyst (CdS/ZnS core-shell nanorods), in which CdS nanorods were modified by dodecylamine and then wrapped by intermittent ZnS shells. Due to the rapid transfer of photogenerated electrons from ZnS shell to CdS nanorods, the adsorption performance of H^+ was improved after dodecylamine modification. The photocatalytic activity was remarkably improved. Supported cocatalyst has been proved to be an effective way to inhibit carrier recombination and reduce reaction overpotential. Precious metals like Au, Pt, Pd, Ag, Ru and their oxides such as RuO_2 are commonly used as cocatalysts for photocatalysis [24–27]. Sun's group [28] synthesized Au nanodots@thiol-UiO-66@$ZnIn_2S_4$ (ZIS) photocatalysts. Au nanodots were anchored in the pores of thiol-functionalized UiO-66, and ZIS nanosheets were wrapped on the metal-organic framework (MOF). In Au@thiol-UiO66@ZIS, photogenerated electrons were transferred from ZIS to MOF, and then to Au nanodots, and a smooth electron transport channel was established. But its high cost and scarcity are not suitable for practical applications. It is necessary to find functional materials with low toxicity, low cost and high efficiency to replace precious metals as cocatalysts for photocatalysis.

Recently, many non-noble metal cocatalysts such as metal nitrides, metal sulfides, metal phosphides and metal carbides have been developed. Among them, molybdenum disulfide has attracted widespread attention in the field of photocatalytic hydrogen evolution [29,30]. Theoretical calculation shows that the moderate adsorption capacity of intermediate hydrogen atoms on MoS_2 and Pt significantly reduces the activation energy of the reaction [31]. In other words, MoS_2 is a promising alternative to Pt. ZIS is widely used for photocatalytic hydrogen production due to its outstanding visible light trapping ability, photostability and low toxicity [32–35]. The combination of ZIS and MoS_2 can effectively promote the separation of electrons and holes. Wei *et al.* [36] prepared ZIS/MoS_2 composites by

[1] State Key Laboratory of Structural Chemistry, Fujian Institute of Research on the Structure of Matter, Chinese Academy of Sciences, Fuzhou 350002, China
[2] University of the Chinese Academy of Sciences, Beijing 100049, China
[3] Fujian Science & Technology Innovation Laboratory for Optoelectronic Information of China, Fuzhou 350108, China
* Corresponding authors (emails: rcao@fjirsm.ac.cn (Cao R); gaosy@fjirsm.ac.cn (Gao S))

impregnating ZIS nanoflowers with $(NH_4)_2MoS_4$ aqueous solution, followed by high-temperature treatment in an H_2S stream to convert Mo(VI) to Mo(IV). This catalyst greatly improves the performance of photocatalytic hydrogen production (141 μmol h^{-1}) due to the increase of charge separation efficiency. Amorphous MoS_2 has been shown to promote photocatalytic activity for the first time. By using a one-pot solvothermal reaction, Zhang *et al.* [37] prepared ZIS/MoS_2 photocatalyst, which significantly improved the photocatalytic H_2 conversion rate of ZIS upon visible light irradiation due to its tight interfacial contact. The introduction of synergistic cocatalyst can further improve the photocatalytic performance of ZIS. Yuan *et al.* [38] synthesized MoS_2-graphene composites as synergistic cocatalyst to promote the photocatalytic activity of ZIS (4167 μmol g^{-1} h^{-1}). The outstanding catalytic activity is ascribed to the unique synergistic effect between MoS_2 and graphene, which function as a co-catalyst and electron transfer channel for hydrogen evolution reactions, respectively. Although MoS_2/ZIS heterojunction has been widely reported, the low charge transfer efficiency between the catalyst and cocatalyst seriously limits the performance of photocatalyst. At present, it is still lacking attempts to improve the efficiency of electron separation by enhancing the interface interaction between the catalyst and cocatalyst. Introducing interfacial chemical bonds to enhance the interfacial interaction between components is an effective means to improve photocatalytic hydrogen production. For example, Li's group [39] synthesized P-doped, MoP-modified g-C_3N_4 (PCN/MoP) heterojunction photocatalysts. The interfacial Mo–N bond serves as an efficiently functioning electron "transfer channel" between PCN and MoP, accelerating the migration and separation of the photogenerated carriers. Shen *et al.* [40] synthesized C_3N_4/WO_3 heterojunction. Theoretical and experimental results confirmed that N–W bond can be used as an atomic interface channel to accelerate the interface electron transfer.

Herein, ZIS/Sv-MoS_2 photocatalyst was synthesized. The binding effect between S atoms in ZIS and the uncoordinated Mo atoms in Sv-MoS_2 forms the interfacial Mo–S bond which greatly improves the photocatalytic activity of ZIS. The interfacial Mo–S bond serves as an efficiently functioning electron "transfer channel" between ZIS and MoS_2, accelerating the migration and separation of the photogenerated carrier. The photocatalytic performance of the optimized ZIS/MoS_2-4h composite was significantly improved. The optimized ZIS/MoS_2-4h composite shows a significant hydrogen production rate of 7.6 mmol g^{-1} h^{-1}, which is approximately 4.75 times that of the original ZIS (1.6 mmol g^{-1} h^{-1}) and 2.05 times that of ZIS/MoS_2 (3.7 mmol g^{-1} h^{-1}). The apparent quantum yield of ZIS/MoS_2-4h is 1.71% at 420 nm (5 mg catalyst).

EXPERIMENTAL SECTION

Preparation of MoS_2

In a typical synthetic procedure, ammonium molybdate tetrahydrate ($(NH_4)_6Mo_7O_{24}{\cdot}4H_2O$) (1.236 g, 1 mmol) and thiourea (CH_4N_2S) (1.0657 g, 14 mmol) were added to 30 mL of deionized water. After stirring for 30 min at room temperature, the resulting solution was transferred to a 50-mL Teflon-lined stainless-steel autoclave and heated at 220°C for 18 h. When the solution was cooled to room temperature, the collected black product was centrifuged, washed several times with deionized water and ethanol and dried under vacuum at 80°C for 12 h.

Preparation of MoS_2-*x*h

The prepared MoS_2 (100 mg) was suspended in 10 mL of aqueous solution and sonicated for 2 h. Then 50 mg $NaBH_4$ was added and further stirred for a certain time (2, 4, and 6 h) at room temperature to obtain MoS_2-*x*h (MoS_2-2h, MoS_2-4h, and MoS_2-6h).

Preparation of ZIS

An aqueous solution of hydrochloric acid (8 mL, pH = 2.5) and glycerol (2 mL) were added into a 25-mL flask and sonicated. Then, after ultrasonic treatment for 30 min and stirring for 5 min, 54.4 mg $ZnCl_2$, 234.4 mg $InCl_3{\cdot}4H_2O$, and 120 mg thioacetamide (TAA) were added. The resulting solution was stirred for 30 min, and then put into an oil bath at 80°C. After 2 h of reaction, the product was collected by centrifugation, washed three times with ethanol and deionized water, and dried in vacuum at 70°C.

Preparation of ZIS/MoS_2 and ZIS/MoS_2-*x*h

ZIS/MoS_2 and ZIS/MoS_2-*x*h were prepared with the same procedure as for ZIS, except that 10 mg of MoS_2 or MoS_2-*x*h was added to the beaker.

Photocatalytic H_2 evolution experiment

The photocatalytic reaction was carried out in a sealed Pyrex top irradiation reactor with a capacity of 180 mL. Photocatalyst (5 mg) was dispersed in 5 mL aqueous solution containing 1 mL of triethanolamine (TEOA) as the sacrificial reagent and continuously stirred until completion. Prior to irradiation, the reaction system was evacuated and purged three times with argon gas to remove all air. The temperature of the reaction was controlled by a circulating condensation system at 25°C. A 300-W Xe lamp with a 420-nm cut-off filter was used to irradiate the suspension. The gas chromatograph (Agilent 7820A) was used to determine the amount of H_2. Usually, 1 mL gas sample was taken from the reaction vessel and injected into the gas chromatograph every one hour.

The apparent quantum efficiency (AQE) of the reaction system was measured using a Xe lamp with light band-pass filter (λ = 420, 450, and 520 nm). The incident monochromatic illumination intensity was measured using the ILT 950 spectroradiometer. The following equation was used to calculate AQE.

$$\mathrm{AQE} = \frac{2MN_Ahc}{AIt\lambda} \times 100\%, \quad (1)$$

where M is the molar amounts of H_2 during 2 h of irradiation, N_A is the Avogadro constant (6.022×10^{23} mol^{-1}), h is the Planck constant (6.626×10^{-34} J s), c is the light velocity (3×10^8 m s^{-1}), A is the irradiation area ($3.14 \times 2.25 \times 10^{-4}$ m^2), I is the intensity of irradiation light (mW cm^{-2}), t is the reaction time (7200 s), and λ is the wavelength of the monochromatic light (nm).

RESULTS AND DISCUSSION

Synthesis and characterization

The preparation process of ZIS/Sv-MoS_2 is depicted in Fig. 1. Firstly, nanoflower-like MoS_2 was synthesized by a hydrothermal method. Then, MoS_2 with rich S vacancies (Sv-MoS_2) was prepared by $NaBH_4$ etching at room temperature (Fig. S1). If the

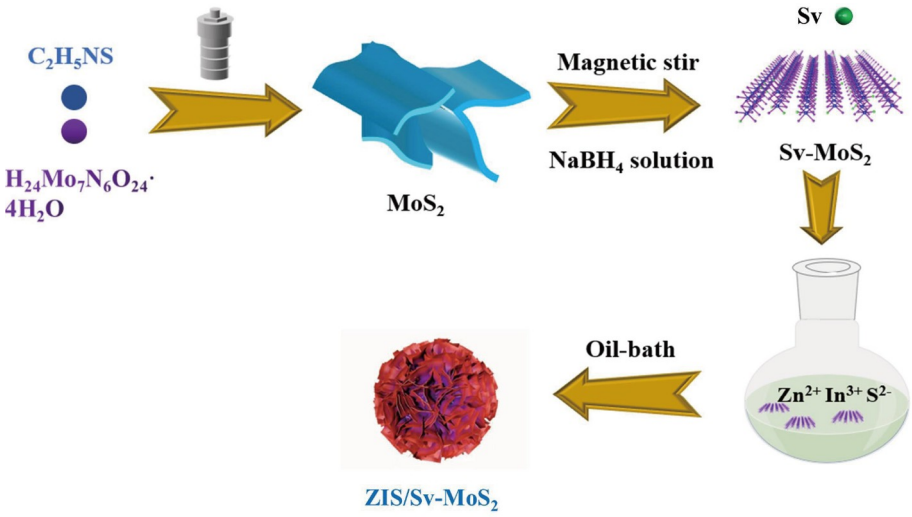

Figure 1 Schematic diagram of the preparation process of ZIS/Sv-MoS_2 heterojunction.

internal structure of MoS_2 is seriously damaged, it will affect the electron transfer, and more defects will also affect the growth process of ZIS. Therefore, we adopted room temperature conditions to avoid more internal defects. Finally, Sv-MoS_2 was immersed in Zn^{2+}, In^{3+}, TAA, and glycerol solution to grow ZIS nanosheets through an oil-bath procedure.

X-ray diffraction (XRD) measurements were implemented to reveal the composition and phase structure of the as-prepared material. The diffraction peaks of bare MoS_2 at 2θ values of 13.94°, 33.36° and 57.53° can be ascribed to the (002), (100) and (110) crystal planes of hexagonal MoS_2 (JCPDS Card No. 87-2416) [41]. With the increase of $NaBH_4$ etching time, the XRD diffraction peak intensity of MoS_2-*x*h decreases, which indicates that the structure becomes more unordered, because MoS_2-*x*h has produced more defects (Fig. 2a). The pure ZIS exhibits three main peaks at 21.48°, 27.90°, and 47.24°, corresponding to (006), (102), and (110) planes of the hexagonal ZIS (JCPDS card No.065-2023) [42]. The characteristic diffraction peaks of ZIS and MoS_2 are clearly shown in the XRD pattern of ZIS/MoS_2-*x*h, which indicates the successful synthesis of ZIS/MoS_2-*x*h composite (Fig. 2b). The microstructure of the samples was also studied by Raman spectroscopy. The pristine MoS_2 shows peaks at 379.3 and 406.0 cm^{-1} attributing to the in-plane E^1_{2g} and out-of-plane A_{1g} [43], which involve anti-parallel vibration of two S atoms relative to Mo atoms, as well as only the vibration of S atom in-plane and out-of-plane in the opposite direction [44]. Compared with MoS_2, the A_{1g} and E^1_{2g} peaks of MoS_2-*x*h are slightly red-shifted. For example, the A_{1g} and E^1_{2g} peaks of MoS_2-4h are shifted to 377.4 and 403.2 cm^{-1}, respectively (Fig. 2c). This phenomenon shows that there is lattice distortion in MoS_2-*x*h, and implies that there are many defects in the catalyst due to a large number of hanging bonds on the surface [45]. This is consistent with the XRD results. In the synthesis of ZIS/MoS_2-4h, the S vacancy in MoS_2-4h will be occupied by the S atom in ZIS. If the interaction between MoS_2-4h and ZIS is weak, the Raman peak of MoS_2-4h in ZIS/ MoS_2-4h will be closer to MoS_2. However, as shown in Fig. 2d, e, the Raman peak of MoS_2 in ZIS/MoS_2-4h moves in the direction of the blue arrow. This shows that there is a strong interaction between MoS_2-4h and ZIS. Electron paramagnetic resonance (EPR) was used to confirm the presence of S vacancies (Fig. 2f). The pristine MoS_2 shows lower EPR intensity with a *g* value of 2.004, which was assigned to the S vacancies on the surface [46]. In contrast, MoS_2-4h shows a sharply increased EPR signal, confirming the presence of a large number of S vacancies in MoS_2-4h. In addition, it is worth noting that the EPR intensity of ZIS/MoS_2-4h significantly decreased compared with MoS_2-4h. This should be due to the binding effect between the S atoms in ZIS and the uncoordinated Mo atoms in MoS_2-4h, reducing the number of unpaired electrons, which forms the interfacial Mo–S bond [47]. As reported in literature, the defect MoS_2 with S vacancy can enhance the photocatalytic activity [44,48]. As can be seen from Fig. 2f, there are few S vacancies in ZIS/MoS_2-4h, which would eliminate the influence of defects on the photocatalytic activity.

Morphology and microstructure of the catalyst were characterized by scanning electron microscopy (SEM). As shown in Fig. 3a, MoS_2 has a nanoflower-like structure, in which the nanosheet size is about 200 nm. The morphology of MoS_2-*x*h has no obvious change compared with MoS_2 (Fig. S2). As shown in Fig. 3b, the pure ZIS exhibits a relatively characteristic nanoflower-like structure with an average diameter of 1–2 μm, consisting mainly of staggered and curled nanosheets. Fig. 3c, d illustrate the SEM images of ZIS/MoS_2-4h, which can be observed that ZIS and MoS_2 are intimately entwined (Fig. S3). The tight interface between materials will promote the transfer and separation of photogenerated charges, thus improving the photocatalytic performance [49,50].

Transmission electron microscopy (TEM) and high-resolution TEM (HRTM) were used to further study the microstructure of the catalysts. When the crystal is defective, the lattice stripes will bend or break, and the defects can be reflected by observing the lattice. Compared with MoS_2, the lattice fringe of MoS_2-4h shows partial bending and fracture, which indicates the existence of defects in MoS_2-4h (Fig. 4a, b and Fig. S4). ZIS and MoS_2 are intimately entwined and a few ZIS nanosheets are located at the surface (Fig. 4c). In the atomic force microscopy image of ZIS/MoS_2-4h, the ultrathin structure can be found (Fig. S5). In Fig. 4d, two different lattice spacings (*d*) are observed, which are 0.32 and 0.62 nm, respectively, ascribed to the (102) plane of hexagonal ZIS and the (002) plane of MoS_2 [51,52]. The energy

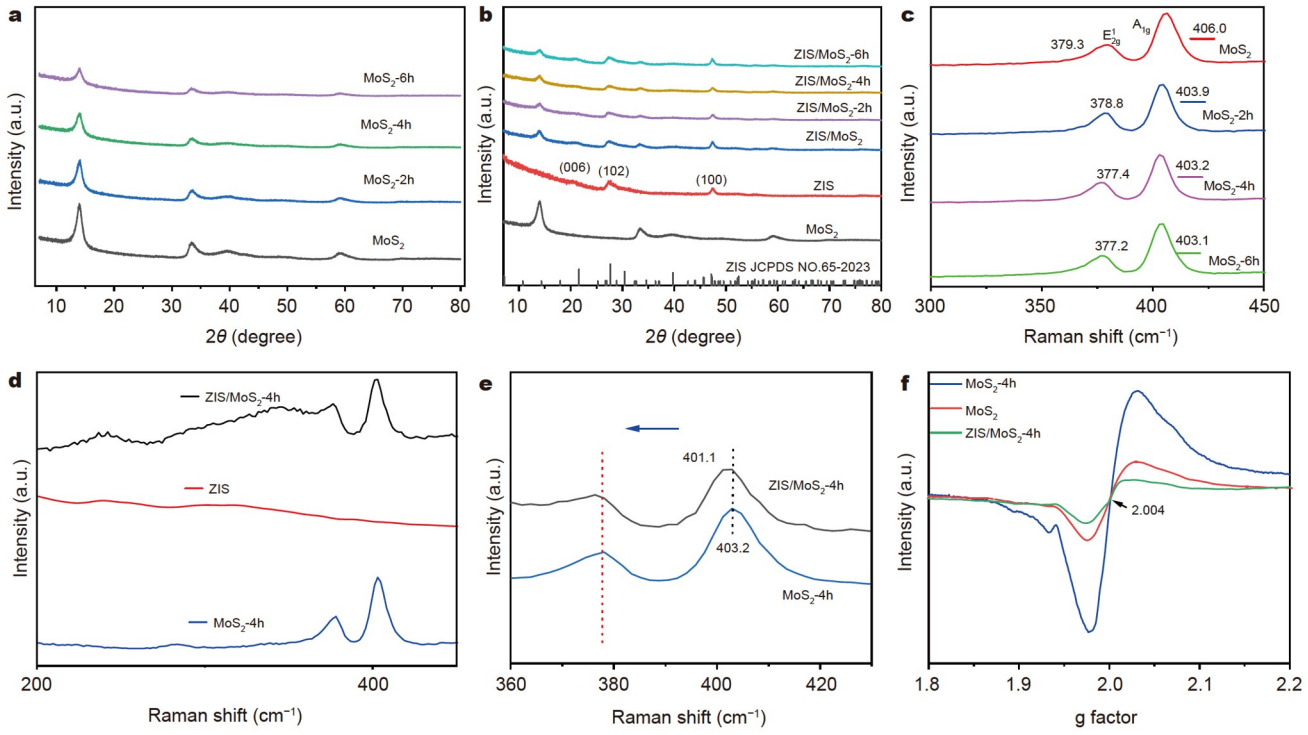

Figure 2 (a) XRD patterns of MoS_2-*x*h; (b) XRD patterns of ZIS and ZIS/MoS_2-*x*h; (c–e) Raman spectra of the as-prepared samples; (f) room-temperature EPR spectra of the samples.

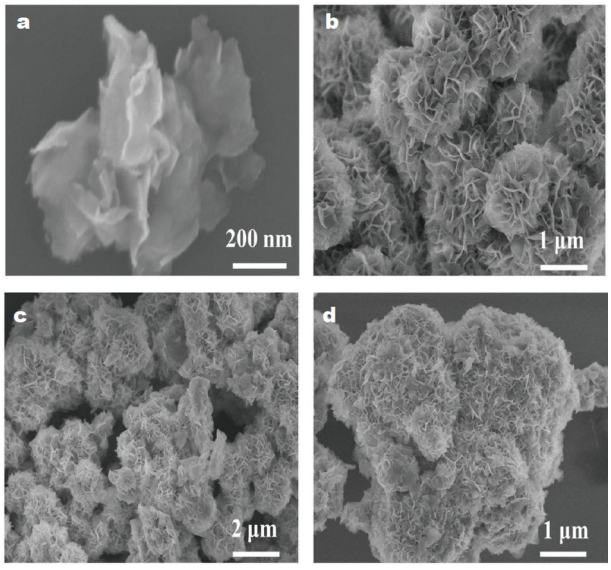

Figure 3 SEM images of (a) MoS_2, (b) ZIS, and (c, d) ZIS/MoS_2-4h.

dispersive X-ray spectroscopy (EDS) element distribution of ZIS/MoS_2-4h was characterized (Fig. 4e). As shown in Fig. 4f, Zn, In and S elements are evenly located in the composite, while Mo elements are largely distributed in the middle, indicating the presence of some ZIS nanosheets on the surface.

The surface composition and chemical state of the catalysts and the interaction between MoS_2-*x*h and ZIS were studied by X-ray photoelectron spectroscopy (XPS). The survey spectrum reveals that Zn, In, S and Mo peaks coexist in ZIS/MoS_2-4h, which is in accordance with the EDS results (Fig. S6a). The Mo 3d signal in MoS_2-4h shows obvious convolution signs, suggesting the unique chemical environment of Mo (Fig. S6b) [53]. The peak of Mo $3d_{3/2}$ for MoS_2-4h is blue shifted compared with

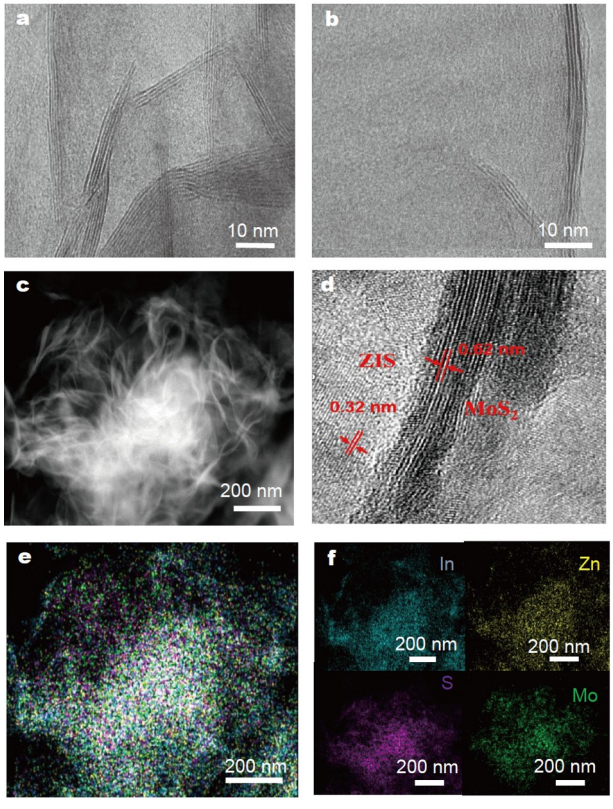

Figure 4 HRTEM images of (a) MoS_2 and (b) MoS_2-4h; (c) TEM image of ZIS/MoS_2-4h; (d) HRTEM image of ZIS/MoS_2-4h; (e, f) EDS mapping images of ZIS/MoS_2-4h.

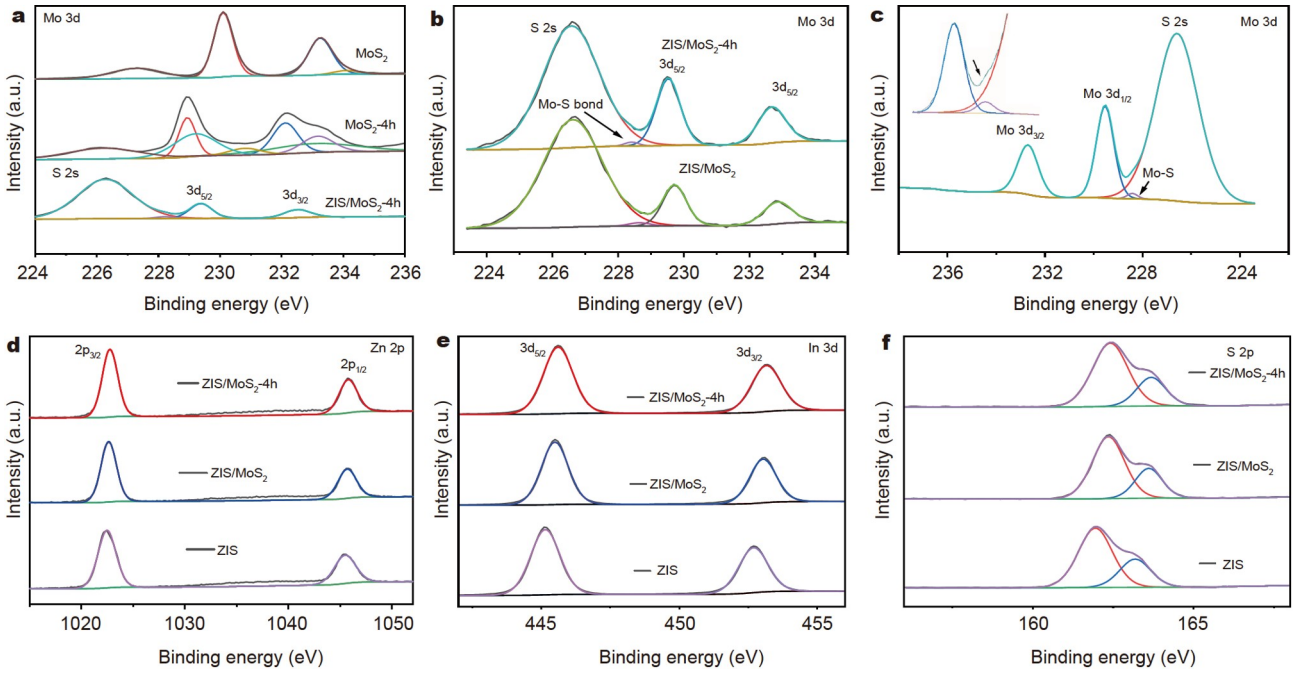

Figure 5 XPS spectra of the as-prepared samples. (a–c) Mo 3d; (d) Zn 2p; (e) In 3d; (f) S 2p.

that of MoS_2, which can be attributable to the decrease of the coordination number of Mo caused by the generation of S vacancy [47]. The Mo 3d signal in ZIS/MoS_2-4h shows similar convolution with MoS_2, which indicates that the combination of S atoms in ZIS and uncoordinated Mo atoms in MoS_2-4h reduces S vacancies, thus forming an interface Mo–S bond. Compared with MoS_2, the XPS peak of Mo $3d_{3/2}$ for ZIS/MoS_2-4h shifts negatively. This shows that there is a strong interaction between ZIS and MoS_2 (Fig. 5a). As shown in Fig. 5b, the XPS peaks of the Mo $3d_{3/2}$ are negatively shifted for ZIS/MoS_2-4h as compared with those of ZIS/MoS_2. Meanwhile, the peak at 228.4 eV verifies the formation of Mo–S bonds as shown in Fig. 5b, c [47]. Because MoS_2 has some S vacancies (Fig. 2f), ZIS/MoS_2 also shows a small peak at 228.2 eV, which is lower than that of ZIS/MoS_2-4h. The peaks of Zn $2p_{3/2}$ and Zn $2p_{1/2}$ for pure ZIS are 1022.46 and 1045.46 eV, respectively, which are consistent with numerous reported literature [54]. When ZIS/MoS_2 composites were formed, the characteristic signals of Zn $2p_{3/2}$ shifted slightly toward higher binding energy. The Zn $2p_{3/2}$ peak of ZIS/MoS_2 is moving to 1022.64 eV, which is 0.18 eV larger than that of the parent ZIS. The Zn $2p_{3/2}$ peak of ZIS/MoS_2-4h was further shifted by 0.12 to 1022.76 eV compared with that of ZIS/MoS_2 (Fig. 5d). The peaks of In $3d_{5/2}$ and In $3d_{3/2}$ for pure ZIS are 445.13 and 452.69 eV, respectively. The In $3d_{5/2}$ peak of ZIS/MoS_2 is moving to 445.49 eV, which is 0.36 eV larger than that of the parent ZIS. The In $3d_{5/2}$ peak of ZIS/MoS_2-4h was further shifted by 0.12 to 445.61 eV compared with that of ZIS/MoS_2 (Fig. 5e). The XPS peaks of the S 2p were positively shifted for ZIS/MoS_2-4h as compared with the ZIS (Fig. 5f). These results confirm that there is a strong interaction between ZIS and MoS_2 in ZIS/MoS_2-4h. It is Mo–S bond that strengthens the connection between MoS_2 and ZIS to facilitate the electron–hole pair separation.

Photocatalytic H_2 evolution

Fig. 6a shows the photocatalytic hydrogen generation performance of ZIS/MoS_2-*x*h using TEOA as a sacrifice agent. The flower-shaped porous ZIS microspheres have photocatalytic activity for hydrogen production, and the H_2 production rate is 1.6 mmol h^{-1} g^{-1}. The optimized ZIS/MoS_2-4h composite shows a significant hydrogen production rate of 7.6 mmol g^{-1} h^{-1}, which is approximately 4.75 times that of the original ZIS (1.6 mmol g^{-1} h^{-1}) and 2.05 times that of the ZIS/MoS_2 (3.7 mmol g^{-1} h^{-1}). However, the decreased activity of ZIS/MoS_2-6h may be due to excessive defects which are not conducive to electron hole separation. Fig. 6b illustrates the photocatalytic hydrogen production performance of ZIS compounded with different masses of MoS_2-4h (5, 10, 15 mg), in which TEOA is used as a hole scavenger. The bare MoS_2 sample is almost inactive. After compounding ZIS with different masses of MoS_2-4h, the optimized photocatalyst, 10 mg ZIS/MoS_2-4h, exhibits a high hydrogen evolution rate of 7.6 mmol g^{-1} h^{-1}. The influence of different sacrificial agents on the photocatalytic performance of ZIS/MoS_2-4h was explored through photocatalysis experiments. As we can see from Fig. 6c, the best H_2 evolution efficiency was found in TEOA solution, indicating that ZIS/MoS_2-4h is highly selective for sacrificial reagents. The ZIS/MoS_2-4h hybrid was found to release H_2 persistently over 10 h (Fig. 6d). The stability of ZIS/MoS_2-4h was assessed by allowing the reaction to proceed for 15 h and calculating the H_2 yield in each 5 h reaction. No obvious deactivation was observed in three sequential cycles (Fig. 6e), indicating the lasting stability of the photocatalyst. The XPS spectrum of the catalyst after the reaction proves the stability of ZIS/MoS_2-4h. After photocatalytic reaction, the peak of Mo 3d XPS decreases, which may be due to the fact that part of the weakly bound MoS_2 is separated from the surface of ZIS and dissolves in the solution. However, the interfacial Mo–S bond (228.3 eV) still exists, which indicates the importance of interfacial Mo–S bond in improving photocatalytic activity. The XPS peaks of In 3d and S 2p shift slightly, which may be due to slight photo-corrosion of the catalyst (Fig. S6c–f). XRD and field emission SEM characterization of the

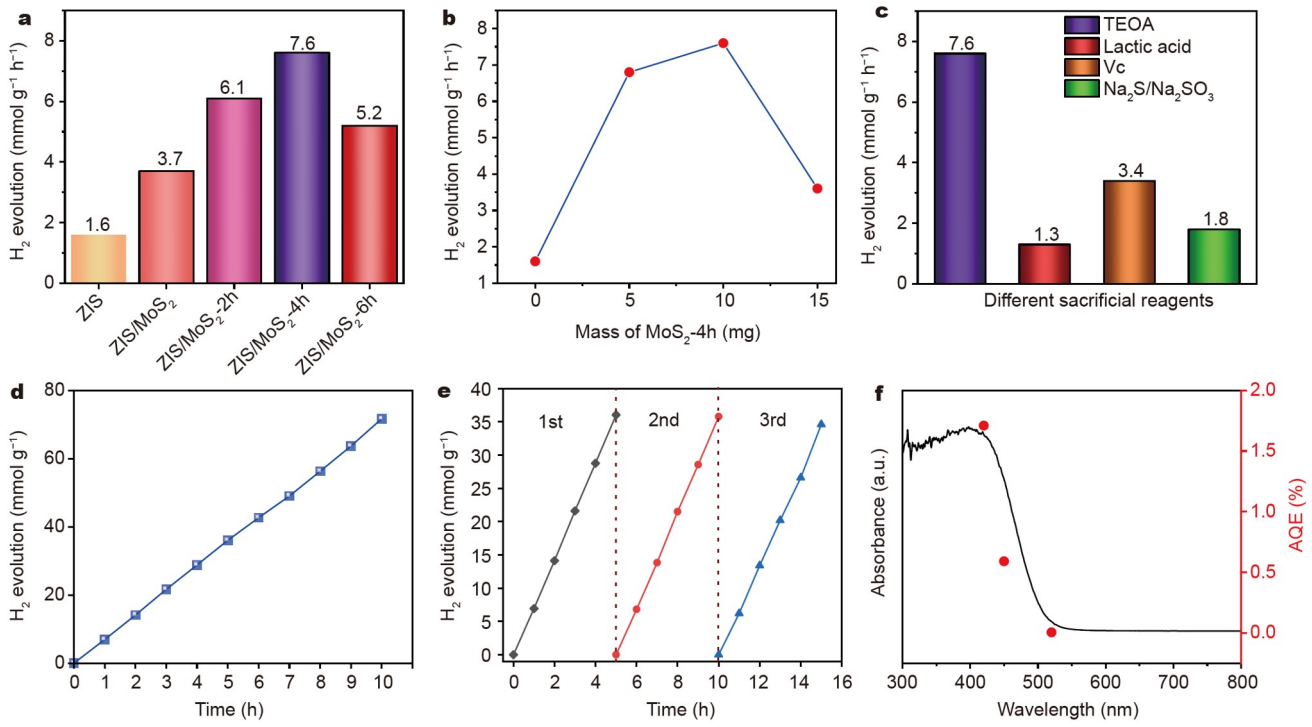

Figure 6 (a) Photocatalytic hydrogen generation performance of 5 mg ZIS/MoS_2-*x*h photocatalyst when ZIS are complexed with 10 mg MoS_2-*x*h; (b) photocatalytic H_2 evolution performance of ZIS compounded with different masses of MoS_2 (5, 10, 15 mg); (c) photocatalytic water splitting performance of ZIS/MoS_2-4h under visible light irradiation ($\lambda \geq 420$ nm) with different hole scavengers; (d, e) stability of photocatalytic H_2 production for ZIS/MoS_2-4h; (f) wavelength-depended AQE of ZIS/MoS_2-4h.

samples after the photocatalytic reaction further support the stability of ZIS/MoS_2-4h (Fig. S7). Fig. 6f shows that the variation of AQE of ZIS/MoS_2-4h is consistent with the absorption spectrum of ZIS, which indicates that ZIS is a photocatalyst and MoS_2 is a cocatalyst for accelerating electron transfer and providing reactive sites (see Table S1 for the specific AQE values of ZIS/MoS_2-4h). This extraordinary photocatalytic activity is mainly responsible for the photogenerated electrons readily shifted from ZIS to MoS_2 across the heterojunction interface between the two materials, which are intimately connected under the action of Mo–S bonds. The H_2 productivity of this work was compared with other recently reported studies (Table S2). This result demonstrates that well-designed co-catalysts have great advantages in improving photocatalytic performance [55,56].

Photoelectrochemical and photoluminescence (PL) measurements

Ultraviolet-visible diffuse reflection absorption spectrum (UV-vis DRS) was used to study the optical absorption characteristics of the samples. The absorption range of MoS_2 spans the entire visible region. The UV-vis DRS of MoS_2-*x*h does not change significantly. However, there are some protrusions in MoS_2-*x*h, which may be caused by Sv [36] (Fig. S8a). ZIS has a strong absorption in the visible region, with absorption edge at 525 nm. Compared with pure ZIS, the absorption of the composite in the visible region is significantly enhanced, which may be due to the absorption of light by MoS_2 (Fig. S8b) [57]. By extrapolating the linear part of $(\alpha h\nu)^{1/2}$ *vs.* photon energy (where α is the absorbance index, h is a constant, and ν is the light frequency), the band gap energy of ZIS is estimated to be 2.58 eV (Fig. S8c). In general, the higher the PL intensity, the higher the probability of photo-generated charge recombination. In order to investigate the transfer efficiency of interfacial electrons from ZIS to MoS_2, the PL spectroscopy was performed. Fig. 7a demonstrates that ZIS exhibits a PL emission peak at about 720 nm. PL intensity of ZIS/MoS_2 hybrids was decreased by the incorporation of MoS_2 nanosheets. Furthermore, PL intensity of the ZIS/MoS_2-4h was drastically reduced, verifying that the recombination of photo-induced electron–hole pairs was suppressed. Therefore, the time-resolved PL (TRPL) images were used to investigate the charge transfer capability of the as-prepared samples. The fluorescence lifetime of ZIS/MoS_2-4h (4.66 ns) is shorter than that of ZIS/MoS_2 (6.09 ns), indicating that the photoinduced electrons of ZIS can be rapidly transferred to MoS_2 in ZIS/MoS_2-4h for H_2 formation (Fig. 7b) [58]. Transient photocurrent responses of ZIS and ZIS/MoS_2-*x*h were compared under visible light irradiation by a 300-W Xe lamp equipped with a cutoff filter ($\lambda > 420$ nm). Fig. 7c shows the photocurrent responses of ZIS and ZIS/MoS_2-*x*h. Among these samples, ZIS presents the lowest photocurrent density due to its severe recombination of photogenerated electron–hole pairs. The ZIS/MoS_2-*x*h exhibits a higher photocurrent, demonstrating that loading cocatalysts can effectively accelerate charge transfer [59]. Notably, the photocurrent of the ZIS/MoS_2-4h composite is the highest, which indicates that there is a strong interface interaction between MoS_2 and ZIS in ZIS/MoS_2-4h. These results show that the photogenerated charge continuously migrates and separates from ZIS to MoS_2 through the heterojunction interface between the two materials, which are closely linked under the action of Mo–S bonds. The charge transfer of the synthetized catalysts was then further investigated by electrochemical impedance spectroscopy (EIS). As shown in Fig. 7d, the arc of ZIS/MoS_2-4h is

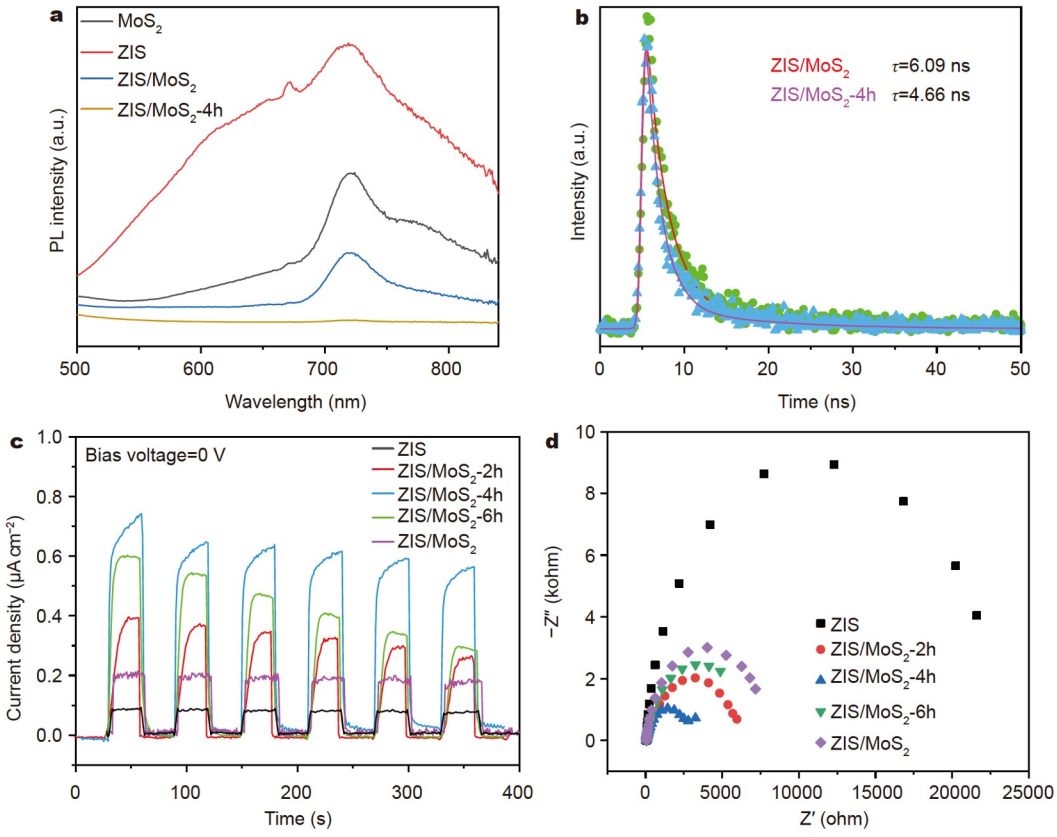

Figure 7 (a) PL spectra of ZIS, ZIS/MoS_2 and ZIS/MoS_2-4h; (b)TRPL spectra of ZIS/MoS_2 and ZIS/MoS_2-4h; (c) transient photocurrent responses; (d) Bode plots of ZIS and ZIS/MoS_2-*x*h.

smaller than that of ZIS and ZIS/MoS_2 [60]. These results show that the Mo–S bond can strengthen the interface interaction of heterojunction and improve the electron separation efficiency of ZIS.

Mechanism analysis

According to the above experimental results, the possible reaction mechanism of photocatalytic hydrogen production of ZIS/MoS_2-4h is proposed in Fig. 8. Under visible light irradiation, the valence band electrons of ZIS are excited to the conduction band, and the flat band potentials of ZIS can be determined by Mott–Schottky measurement (Fig. S8d). According to the formulas E(NHE) = E(Ag/AgCl) + 0.197 and E(ZIS *vs.* Ag/AgCl) = −0.88 eV (E(NHE) is the standard hydrogen electrode potential) (Fig. S8d), the E_{CB} value of ZIS is estimated to be −0.68 eV. The E_{VB} value of ZIS was calculated to be 1.90 eV according to the formula $E_{VB} = E_{CB} + E_g$ (where E_{VB} refers to valence band, E_{CB} refers to conduction band and E_g is the band gap) because of the low Fermi energy level of MoS_2 [46]. Thermodynamically, the photogenerated electrons are readily transferred from ZIS to MoS_2 through the heterojunction interface between the two materials, which are closely linked under the action of Mo–S bonds. MoS_2 acts as a photogenic electron acceptor and inhibits electron hole recombination. The electrons on MoS_2 will reduce H_2O to H_2. In the meantime, the holes on ZIS are consumed by the sacrificial agent. Photoelectric measurements show that ZIS/MoS_2-4h has effective charge transfer. The results show that the Mo–S bond can strengthen the interface interaction of heterojunction and improve the electron separation efficiency of ZIS.

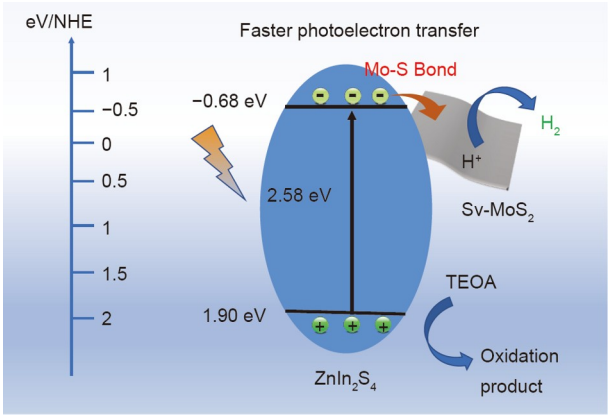

Figure 8 Possible mechanism of photocatalytic hydrogen evolution of ZIS/MoS_2-4h under visible light.

CONCLUSION

In summary, MoS_2 with rich S vacancies was prepared by $NaBH_4$ etching, which improved the photocatalytic H_2 evolution activity of ZIS. The binding effect between S in ZIS and the uncoordinated Mo in Sv-MoS_2 forms the interfacial Mo–S bond. Introducing interfacial chemical bonds to enhance the interfacial interaction between components is an effective means to improve photocatalytic hydrogen production. The optimized ZIS/MoS_2-4h composite shows a significant hydrogen production rate of 7.6 mmol g^{-1} h^{-1}, which is approximately 4.75 times that of the original ZIS (1.6 mmol g^{-1} h^{-1}) and 2.05 times that of

the ZIS/MoS_2 (3.7 mmol g^{-1} h^{-1}) and its photocatalytic activity remains unchanged after three cycles for 15 h. The improvement of activity and stability of ZIS/MoS_2-4h is due to the fact that photogenerated electrons are easily transferred from ZIS to MoS_2 through the tightly connected heterojunction interface under the action of Mo–S bond. This work reveals the influence of interface chemical bonds on the photocatalytic activity of ZIS/MoS_2, and provides a simple and effective method for designing excellent photocatalytic cocatalysts through interface engineering.

Received 14 January 2023; accepted 21 March 2023; published online 30 June 2023

1 Xing F, Zeng R, Cheng C, *et al.* POM-incorporated $ZnIn_2S_4$ Z-scheme dual-functional photocatalysts for cooperative benzyl alcohol oxidation and H_2 evolution in aqueous solution. Appl Catal B-Environ, 2022, 306: 121087
2 Nikoloudakis E, López-Duarte I, Charalambidis G, *et al.* Porphyrins and phthalocyanines as biomimetic tools for photocatalytic H_2 production and CO_2 reduction. Chem Soc Rev, 2022, 51: 6965–7045
3 Simon T, Bouchonville N, Berr MJ, *et al.* Redox shuttle mechanism enhances photocatalytic H_2 generation on Ni-decorated CdS nanorods. Nat Mater, 2014, 13: 1013–1018
4 Maeda K, Teramura K, Lu D, *et al.* Photocatalyst releasing hydrogen from water. Nature, 2006, 440: 295
5 Wang Y, Zhang Z, Li J, *et al.* Two-dimensional-on-three-dimensional metal-organic frameworks for photocatalytic H_2 production. Angew Chem Int Ed, 2022, 61: e202211031
6 Lu Y, Yin WJ, Peng KL, *et al.* Self-hydrogenated shell promoting photocatalytic H_2 evolution on anatase TiO_2. Nat Commun, 2018, 9: 2752
7 Xing W, Tu W, Han Z, *et al.* Template-induced high-crystalline g-C_3N_4 nanosheets for enhanced photocatalytic H_2 evolution. ACS Energy Lett, 2018, 3: 514–519
8 Yuan YJ, Yu ZT, Chen DQ, *et al.* Metal-complex chromophores for solar hydrogen generation. Chem Soc Rev, 2017, 46: 603–631
9 Xu M, Li D, Sun K, *et al.* Interfacial microenvironment modulation boosting electron transfer between metal nanoparticles and MOFs for enhanced photocatalysis. Angew Chem Int Ed, 2021, 60: 16372–16376
10 Mao S, Shi JW, Sun G, *et al.* PdS quantum dots as a hole attractor encapsulated into the MOF@$Cd_{0.5}Zn_{0.5}S$ heterostructure for boosting photocatalytic hydrogen evolution under visible light. ACS Appl Mater Interfaces, 2022, 14: 48770–48779
11 Zhang M, Qin C, Sun W, *et al.* Energy funneling and charge separation in CdS modified with dual cocatalysts for enhanced H_2 generation. Chin J Catal, 2022, 43: 1818–1829
12 Vamvasakis I, Papadas IT, Tzanoudakis T, *et al.* Visible-light photocatalytic H_2 production activity of β-Ni(OH)$_2$-modified CdS mesoporous nanoheterojunction networks. ACS Catal, 2018, 8: 8726–8738
13 Xiang X, Zhu B, Cheng B, *et al.* Enhanced photocatalytic H_2-production activity of CdS quantum dots using Sn^{2+} as cocatalyst under visible light irradiation. Small, 2020, 16: 2001024
14 Cui C, Zhao X, Su X, *et al.* Porphyrin-based donor-acceptor covalent organic polymer/$ZnIn_2S_4$ Z-scheme heterostructure for efficient photocatalytic hydrogen evolution. Adv Funct Mater, 2022, 32: 2208962
15 Zhou D, Xue X, Wang X, *et al.* Ni, In co-doped $ZnIn_2S_4$ for efficient hydrogen evolution: Modulating charge flow and balancing H adsorption/desorption. Appl Catal B-Environ, 2022, 310: 121337
16 Yang W, Zhang L, Xie J, *et al.* Enhanced photoexcited carrier separation in oxygen-doped $ZnIn_2S_4$ nanosheets for hydrogen evolution. Angew Chem Int Ed, 2016, 55: 6716–6720
17 Ma K, Zhang M, Sun W, *et al.* Revealing different depth boron substitution on interfacial charge transfer in TiO_2 for enhanced visible-light H_2 production. Appl Catal B-Environ, 2022, 315: 121570
18 Tan M, Yu C, Zeng H, *et al. In situ* fabrication of MIL-68(In)@$ZnIn_2S_4$ heterojunction for enhanced photocatalytic hydrogen production. Nanoscale, 2023, 15: 2425–2434
19 Guan Z, Pan J, Li Q, *et al.* Boosting visible-light photocatalytic hydrogen evolution with an efficient $CuInS_2$/$ZnIn_2S_4$ 2D/2D heterojunction. ACS Sustain Chem Eng, 2019, 7: 7736–7742
20 Chen Z, Guo F, Sun H, *et al.* Well-designed three-dimensional hierarchical hollow tubular g-C_3N_4/$ZnIn_2S_4$ nanosheets heterostructure for achieving efficient visible-light photocatalytic hydrogen evolution. J Colloid Interface Sci, 2020, 607: 1391–1401
21 Liang Q, Gao W, Liu C, *et al.* A novel 2D/1D core-shell heterostructures coupling MOF-derived iron oxides with $ZnIn_2S_4$ for enhanced photocatalytic activity. J Hazard Mater, 2020, 392: 122500
22 Jiang R, Mao L, Zhao Y, *et al.* 1D/2D CeO_2/$ZnIn_2S_4$ Z-scheme heterojunction photocatalysts for efficient H_2 evolution under visible light. Sci China Mater, 2023, 66: 139–149
23 Sun G, Shi JW, Mao S, *et al.* Dodecylamine coordinated tri-arm CdS nanorod wrapped in intermittent ZnS shell for greatly improved photocatalytic H_2 evolution. Chem Eng J, 2022, 429: 132382
24 Wang X, Sun K, Gu S, *et al.* Construction of a novel electron transfer pathway by modifying $ZnIn_2S_4$ with α-MnO_2 and Ag for promoting solar H_2 generation. Appl Surf Sci, 2021, 549: 149341
25 Liu X, Wang S, Yang F, *et al.* Construction of Au/g-C_3N_4/$ZnIn_2S_4$ plasma photocatalyst heterojunction composite with 3D hierarchical microarchitecture for visible-light-driven hydrogen production. Int J Hydrogen Energy, 2022, 47: 2900–2913
26 Zhang J, Yang G, He B, *et al.* Electron transfer kinetics in CdS/Pt heterojunction photocatalyst during water splitting. Chin J Catal, 2022, 43: 2530–2538
27 Cao B, Li G, Li H. Hollow spherical RuO_2@TiO_2@Pt bifunctional photocatalyst for coupled H_2 production and pollutant degradation. Appl Catal B-Environ, 2016, 194: 42–49
28 Mao S, Shi JW, Sun G, *et al.* Au nanodots@thiol-UiO_{66}@$ZnIn_2S_4$ nanosheets with significantly enhanced visible-light photocatalytic H_2 evolution: The effect of different Au positions on the transfer of electron-hole pairs. Appl Catal B-Environ, 2021, 282: 119550
29 Liang Z, Shen R, Ng YH, *et al.* A review on 2D MoS_2 cocatalysts in photocatalytic H_2 production. J Mater Sci Tech, 2020, 56: 89–121
30 Guo L, Yang Z, Marcus K, *et al.* MoS_2/TiO_2 heterostructures as nonmetal plasmonic photocatalysts for highly efficient hydrogen evolution. Energy Environ Sci, 2018, 11: 106–114
31 He J, Chen L, Wang F, *et al.* CdS nanowires decorated with ultrathin MoS_2 nanosheets as an efficient photocatalyst for hydrogen evolution. ChemSusChem, 2016, 9: 624–630
32 Jia WL, Wu X, Liu Y, *et al.* Porous $ZnIn_2S_4$ with confined sulfur vacancies for highly efficient visible-light-driven photocatalytic H_2 production. J Mater Chem A, 2022, 10: 25586–25594
33 Peng X, Li J, Yi L, *et al.* Ultrathin $ZnIn_2S_4$ nanosheets decorating PPy nanotubes toward simultaneous photocatalytic H_2 production and 1,4-benzenedimethanol valorization. Appl Catal B-Environ, 2022, 300: 120737
34 Liu H, Zhang J, Ao D. Construction of heterostructured $ZnIn_2S_4$@NH_2-MIL-125(Ti) nanocomposites for visible-light-driven H_2 production. Appl Catal B-Environ, 2018, 221: 433–442
35 Wang P, Fan S, Li X, *et al.* Piezotronic effect and hierarchical Z-scheme heterostructure stimulated photocatalytic H_2 evolution integrated with C–N coupling of benzylamine. Nano Energy, 2021, 89: 106349
36 Wei L, Chen Y, Lin Y, *et al.* MoS_2 as non-noble-metal co-catalyst for photocatalytic hydrogen evolution over hexagonal $ZnIn_2S_4$ under visible light irradiations. Appl Catal B-Environ, 2014, 144: 521–527
37 Zhang Z, Huang L, Zhang J, *et al. In situ* constructing interfacial contact MoS_2/$ZnIn_2S_4$ heterostructure for enhancing solar photocatalytic hydrogen evolution. Appl Catal B-Environ, 2018, 233: 112–119
38 Yuan YJ, Tu JR, Ye ZJ, *et al.* MoS_2-graphene/$ZnIn_2S_4$ hierarchical microarchitectures with an electron transport bridge between light-harvesting semiconductor and cocatalyst: A highly efficient photocatalyst for solar hydrogen generation. Appl Catal B-Environ, 2016, 188: 13–22
39 Wang X, Wang X, Tian W, *et al.* High-energy ball-milling constructing P-doped g-C_3N_4/MoP heterojunction with Mo–N bond bridged interface and Schottky barrier for enhanced photocatalytic H_2 evolution. Appl Catal B-Environ, 2022, 303: 120933

40 Shen R, Zhang L, Li N, *et al.* W–N bonds precisely boost Z-scheme interfacial charge transfer in g-C_3N_4/WO_3 heterojunctions for enhanced photocatalytic H_2 evolution. ACS Catal, 2022, 12: 9994–10003
41 Tian Y, Ge L, Wang K, *et al.* Synthesis of novel MoS_2/g-C_3N_4 heterojunction photocatalysts with enhanced hydrogen evolution activity. Mater Charact, 2014, 87: 70–73
42 Li X, Wang X, Zhu J, *et al.* Fabrication of two-dimensional Ni_2P/$ZnIn_2S_4$ heterostructures for enhanced photocatalytic hydrogen evolution. Chem Eng J, 2018, 353: 15–24
43 Liao W, Xie K, Liu L, *et al.* Triggering in-plane defect cluster on MoS_2 for accelerated dinitrogen electroreduction to ammonia. J Energy Chem, 2021, 62: 359–366
44 Ye G, Gong Y, Lin J, *et al.* Defects engineered monolayer MoS_2 for improved hydrogen evolution reaction. Nano Lett, 2016, 16: 1097–1103
45 Nan H, Wang Z, Wang W, *et al.* Strong photoluminescence enhancement of MoS_2 through defect engineering and oxygen bonding. ACS Nano, 2014, 8: 5738–5745
46 Luo N, Chen C, Yang D, *et al.* S defect-rich ultrathin 2D MoS_2: The role of S point-defects and S stripping-defects in the removal of Cr(VI) *via* synergistic adsorption and photocatalysis. Appl Catal B-Environ, 2021, 299: 120664
47 Wang X, Wang X, Huang J, *et al.* Interfacial chemical bond and internal electric field modulated Z-scheme Sv-$ZnIn_2S_4$/$MoSe_2$ photocatalyst for efficient hydrogen evolution. Nat Commun, 2021, 12: 4112
48 Fang Z, Huang X, Wang Y, *et al.* Dual-defective strategy directing *in situ* assembly for effective interfacial contacts in MoS_2 cocatalyst/In_2S_3 light harvester layered photocatalysts. J Mater Chem A, 2016, 4: 13980–13988
49 He K, Xie J, Li M, *et al. In situ* one-pot fabrication of g-C_3N_4 nanosheets/NiS cocatalyst heterojunction with intimate interfaces for efficient visible light photocatalytic H_2 generation. Appl Surf Sci, 2018, 430: 208–217
50 Lu X, Che W, Hu X, *et al.* The facile fabrication of novel visible-light-driven Z-scheme $CuInS_2$/Bi_2WO_6 heterojunction with intimate interface contact by *in situ* hydrothermal growth strategy for extraordinary photocatalytic performance. Chem Eng J, 2019, 356: 819–829
51 Wang S, Guan BY, Wang X, *et al.* Formation of hierarchical Co_9S_8@$ZnIn_2S_4$ heterostructured cages as an efficient photocatalyst for hydrogen evolution. J Am Chem Soc, 2018, 140: 15145–15148
52 Wang H, Naghadeh SB, Li C, *et al.* Enhanced photoelectrochemical and photocatalytic activities of CdS nanowires by surface modification with MoS_2 nanosheets. Sci China Mater, 2018, 61: 839–850
53 Zhang J, Tian X, Liu M, *et al.* Cobalt-modulated molybdenum-dinitrogen interaction in MoS_2 for catalyzing ammonia synthesis. J Am Chem Soc, 2019, 141: 19269–19275
54 Jia WL, Li WJ, Yuan HY, *et al.* Surface Cu^+ modified $ZnIn_2S_4$ for promoted visible-light photocatalytic hydrogen evolution. J Energy Chem, 2022, 74: 341–348
55 Xiao M, Zhang L, Luo B, *et al.* Molten-salt-mediated synthesis of an atomic nickel co-catalyst on TiO_2 for improved photocatalytic H_2 evolution. Angew Chem, 2020, 132: 7297–7301
56 Ren X, Li C, Liu J, *et al.* The fabrication of Pd single atoms/clusters on COF layers as co-catalysts for photocatalytic H_2 evolution. ACS Appl Mater Interfaces, 2022, 14: 6885–6893
57 Zang S, Zhang G, Lan ZA, *et al.* Enhancement of photocatalytic H_2 evolution on pyrene-based polymer promoted by MoS_2 and visible light. Appl Catal B-Environ, 2019, 251: 102–111
58 Xu J, Yan X, Qi Y, *et al.* Novel phosphidated MoS_2 nanosheets modified CdS semiconductor for an efficient photocatalytic H_2 evolution. Chem Eng J, 2019, 375: 122053
59 Ding D, Jiang Z, Ji D, *et al.* Bi_2O_2Se as a novel co-catalyst for photocatalytic hydrogen evolution reaction. Chem Eng J, 2020, 400: 125931
60 Li Y, Wang L, Cai T, *et al.* Glucose-assisted synthesize 1D/2D nearly vertical CdS/MoS_2 heterostructures for efficient photocatalytic hydrogen evolution. Chem Eng J, 2017, 321: 366–374

Acknowledgements This work was supported by the National Key Research and Development Program of China (2021YFA1501500), the National Natural Science Foundation of China (22033008, 22220102005, and 22171265), and Fujian Science & Technology Innovation Laboratory for Optoelectronic Information of China (2021ZZ103).

Author contributions Gao S and Ye S designed and engineered the experiments; Ye S performed the experiments and the characterizations; Ye S wrote the paper with support from Gao S and Cao R. All authors contributed to the general discussion.

Conflict of interest The authors declare that they have no conflict of interest.

Supplementary information Experimental details and supporting data are available in the online version of the paper.

Shihua Ye is currently a Master student at Fujian Institute of Research on the Structure of Matter, Chinese Academy of Sciences (FJIRSM, CAS).

Shuiying Gao received her Master degree from Lanzhou Institute of Chemical Physics, CAS in 2002. She obtained her PhD degree from FJIRSM, CAS, in 2006. In 2014, she became a professor of FJIRSM. Her research interest focuses on thin-film materials and photocatalysis.

Rong Cao obtained his PhD degree from FJIRSM, CAS, in 1993. Following post-doctoral experience at the Hong Kong Polytechnic University and JSPS Fellowship at Nagoya University, he became a professor of FJIRSM in 1998. Now, he is the director of FJIRSM. His main research interests include supramolecular chemistry, inorganic-organic hybrid materials and nanocatalysts.

构建具有微妙的原子级紧密接触的$ZnIn_2S_4$/Sv-MoS_2光催化剂: 增强界面相互作用以改善可见光下的光催化产氢性能

叶士华[1,2,3], 李静君[1,2,3], 冯亚男[1], 高水英[1,2,3*], 曹荣[1,2,3*]

摘要 催化剂与助催化剂之间的低电荷分离效率严重限制了光催化性能. 催化剂与助催化剂之间的强界面相互作用可以提高电荷分离效率. 通过引入界面化学键增强组分间的界面相互作用是提高光催化性能的有效手段之一. 本文合成了$ZnIn_2S_4$ (ZIS)/Sv-MoS_2光催化剂, ZIS中的S原子与Sv-MoS_2中未配位Mo原子之间的键合作用形成了界面Mo–S键, 这极大地提高了ZIS的光催化活性. 采用不同的$NaBH_4$蚀刻时间制备了MoS_2-*x*h. 优化后的ZIS/MoS_2-4h复合材料的产氢速率为7.6 mmol g^{-1} h^{-1}, 是原ZIS (1.6 mmol g^{-1} h^{-1})的4.75倍, 是ZIS/MoS_2 (3.7 mmol g^{-1} h^{-1})的2.05倍. 非凡的光催化活性可归因于光生电子在Mo–S键的作用下更容易从ZIS转移到MoS_2. 光电测量表明, ZIS/MoS_2-4h具有有效的电荷转移. 本工作揭示了引入界面化学键对ZIS/MoS_2光催化活性的影响, 为通过界面工程设计优良的助催化剂提供了一种简单有效的方法.

